According to the project proposal, in the stage **IV/2015** of this project the following objectives were approached and solved:

O1/ Identification of parameters affecting the physico-chemical properties of non-noble bimetallic (Co and Ni) nanoparticles supported on SBA-15mesoporous silica.

A1.1. Preparation of CoNi/SBA-15 materials by MDI method.

A1.2. Preparation of CoNi/SBA-15 samples with various M1:M2 ratios

In this stage, taking into account the previous results, our studies have been extended to the deposition of cobalt and nickel bimetallic nanoparticles on mesoporous silica supports of SBA-15 type with optimized textural properties. SBA-15 used as support was calcined under controlled temperature then stored under controlled humidity till preparing supported catalysts by MDI method. The metal loading degree was 5 wt. %. In this tage, our studies were directed towards the preparation of mono-metallic Co/SBA-15 and Ni/SBA-15 (Activity A1.1), then towards the effect of mass ratios M1:M2 (M1 = cobalt, M2 = nickel; M1:M2 = 8:2, 5:5, 2:8; M = 5 wt %) (Activity A1.2) on the physico-chemical properties of bimetallic CoNi/SBA=15 systems.

Cobalt and nickel nitrates were used as metallic precursors. Samples obtained by MDI method were dried at 25 °C for 48 h then calcined at 500 °C (heating rate of 1.5 °C/min, 6 h at final temperature).

O2/ Advanced characterization of CoNi/SBA-15 materials

A2.1. Characterization of CoNi/SBA-15 samples in relation to their structural and textural properties

A2.1. Characterization of CoNi/SBA-15 samples in relation to the bulk and surface chemical composition

After calcination, CoNi/SBA-15 materials obtained by MDI were analyzed in relation to the structure, texture, bulk and surface chemical composition, optical properties and electronic structure, by various techniques as: ICP-OES, EDX, DRX (small and large angles), N_2 physisorption, TEM, and DRUV-Vis.

Selection of the most significant results

Table 1 collects the data obtained from chemical analysis and XRD at small and large angles. According to the ICP-OES analysis, the mass percents for samples of CoNi/SBA-15 type are close to the calculated ones, both in terms of the amount of metal relative to support, and mass ratios between the two metals. Figure 1 illustrates the diffractograms registered at small angles (Figure 1A, B) from which the degree of ordering of SBA-15 silica, both parent and loaded with metal oxides, was evaluated.

All the diffractograms show the (100), (110), and (200) diffraction planes, typically for ordered mesoporous materials with cylindrical and parallel pores, with hexagonal symmetry of *p6mm* type. Moreover, the degree of ordering at long range is very good, as it is proved by the presence of (210) and (300) diffraction planes at 2 theta between 2 and 3° (Figure 1B).
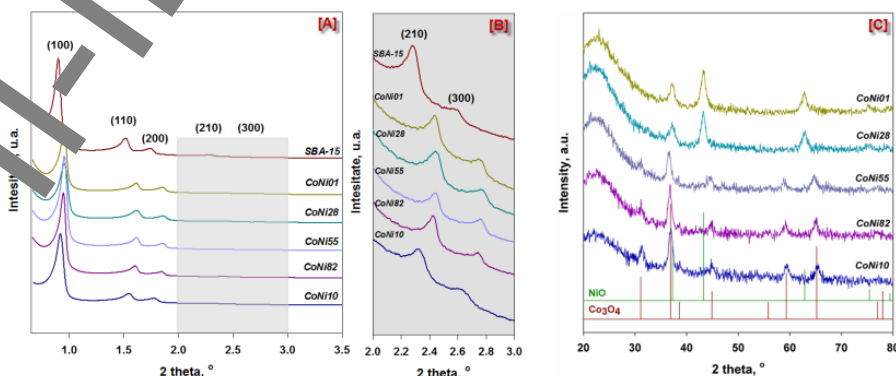

Fig. 1. XRD patterns at small angles (A,B) and large angles (C) for calcined samples of CoNi/SBA-15 type.

On the basis of these diffractograms, the values of interplanar distances, d_{100}, and unit cell parameters, a_0, (Table 1) were evaluated, which are in agreement to the previous published data [1]. As general remark, on

observes that the values of these parameters are slightly diminished after loading of SBA-15 support by Co and Ni nitrate precursors as consequence of the presence of metal oxide particles inside the support pores. The identification of oxide phases obtained by calcination of the deposited precursors (by MDI method) on SBA-15 surface was realized on the basis of diffractograms registered at high angles, between 20 and 80° (Figure 1C). The diffractograms for monocomponent samples of Ni/SBA-15 (CoNi01) and Co/SBA-15 (CoNi10) type show diffraction peaks corresponding to the oxide phases of NiO type (ICDD 047-1049) and Co_3O_4 (ICDD 042-1467), respectively. By applying Scherrer's equation the average size of oxide crystallites were evaluated (Table 1), which is very close of the value of mesopores diameter suggesting confinement of NPs inside the pores. In the case of samples containing predominantly Ni or Co (i.e., CoNi28 and CoNi82, respectively), the identified crystalline phases correspond to the main element. Thus, for CoNi28 sample, the diffraction peaks correspond to NiO phase, while for CoNi82 sample the crystalline phases are of Co_3O_4 type.

Tabel 1. Structural properties and chemical compositions of SBA-15 support and calcined CoNi/SBA-15 materials.

Sample	ICP		XRD small angles		XRD large angles		
	Co wt. %	Ni wt. %	d_{100}[a] (nm)	a_o[b] (nm)	D_{Co3O4}[c] (nm)	D_{NiO}[c] (nm)	$D_{C...O4}$[c] (nm)
SBA-15	-	-	9.9	11.4	-	-	-
CoNi01	-	4.94	9.3	10.7	-	~4	-
CoNi28	0.98	4.63	9.4	10.8	-	7.9	-
CoNi55	2.72	3.09	9.4	10.8	-	-	10.4
CoNi82	5.29	1.66	9.4	10.8	11.1	-	-
CoNi10	5.21	-	9.7	11.2	13.7	-	-

[a]d_{100} interplanar distances; [b]$a_0 = 2d_{100}/\sqrt{3}$. [c]crystallite size calculated by Scherrer's equation: $d_{hkl} = K(\lambda/\beta)\cos\theta$.

The difractogram of sample with similar content of Ni and Co (CoNi55) shows diffraction peaks slightly shifted towards small values, by comparison to pure Co_3O_4 phase, indicating the formation of new crystalline phase. On the basis of quantitative analysis, this phase was identified as belonging to the spinel of $NiCo_2O_4$ type (see also ICDD 20-0781). Therefore, it could be asserted that such mass ratio favors the migration of Ni atoms in the octahedral sites of the network of spinel type, while the Co atoms will be distributed between the octahedral and tetrahedral sites [2].

The porosity of these materials was evaluated by nitrogen physisorption. The registered isotherms are collected in Figure 2A. As first remark, it could be noted that the isotherms are of type IV with hysteresis of H1 type, typically for SBA-15 mesostructured materials. Size pores distribution (Figure 2B) is narrow having maximum at 8.0 nm. It is interesting to observe the fact that the desorption branch corresponding to the samples containing metallic oxides shows a slight delay in closing the loop, phenomenon generally associated with the formation of new mesopores of *ink-bottle* type. As previously shown [3, 4], such type of pores are formed by partial blocking of the main pores with nanoparticles having similar diameter to the pores, phenomenon known as "confinement" of nanoparticles. As consequence of such blocking, a new maxima at 7.3 nm (sample CoNi28) and 6.7 nm (for the rest) appeared. This maximum is becoming sharper by increasing the amount of cobalt in the sample.
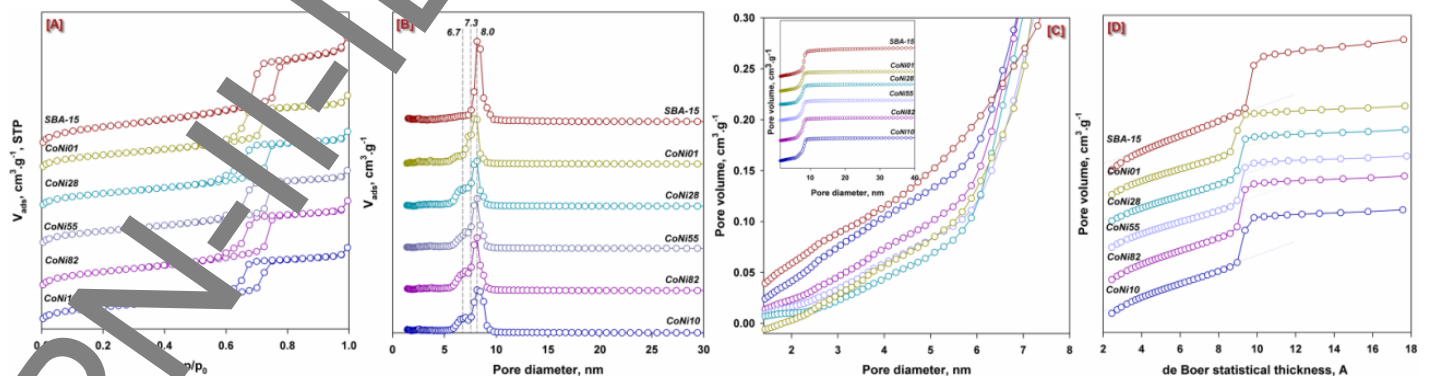

Fig. 2. Nitrogen adsorption-desorption isotherms (A), pores size distribution curves based on NL-DFT method (B), CPV (C) and *t*-plot (D) for calcined samples of type CoNi/SBA-15 and SBA-15 support.

By applying of the specific algorithms, the values of textural properties were evaluated and collected in Table 2. As expected, the values corresponding to the samples loaded by metallic oxides are lower than

those corresponding to SBA-15 support. Another interesting aspect consists of the modification of the values of pores volume and surface. Mainly, this is attributed to the additional porosity developed in silica walls during synthesis of SBA-5, when the polyethyleneoxide branch of P123 located outside of surfactant micelles will be surrounded by silica network and captured within silica structure. By calcination, these organic moieties are destroyed and such a secondary micro- and mesoporosity will form [5]. This secondary porosity can be evaluated both by *t*-plot representation (Figure 1D) and by means of cumulated volume (*cumulativ pore volume-CPV*, Figure 1C).

Table 2. Textural properties of SBA-15 support and calcined CoNi/SBA-15 materials.

Sample	S_{BET}[a] $(m^2.g^{-1})$	S_{mezo}[b] $(m^2.g^{-1})$	S_μ[c] $(m^2.g^{-1})$	V_p[d] $(cm^3.g^{-1})$	V_μ[e] $(cm^3.g^{-1})$	Dp[f] (nm)
SBA-15	858	194	195	1.34	0.090	8.0
CoNi01	616	530	103	0.91	0.043	7.3; 8.0
CoNi28	608	533	91	0.93	0.035	6.7; 8.0
CoNi55	619	546	106	0.93	0.042	6.7; 8.0
CoNi82	720	638	140	1.07	0.059	6.7; 8.0
CoNi10	760	676	186	1.08	0.082	6.7; 8.0

[a]S_{BET} = specific surface evaluated by BET equation ($P/P_0 = 0.1-0.25$). [b]S_{mezo} = mesopores surface evaluated by *t*-plot; [c]S_μ si [e]V_μ = pore surface and volume evaluated by *t*-plot; [d]V_{total} = pore volume evaluated at $P/P_0 = 0.97$; [f]Dp = pores diameter evaluated by NLDFT method applied for cylindrical pores.

Comparing the results obtained by the two methods, it observes a certain incongruity among them (Table 3). Thus, the values calculated by *t*-plot method for samples containing metallic oxides are greater than those obtained by CPV method. This inadvertence originates in the extrinsic porosity of support and it could be attributed to the forming of supplementary porosity in oxide crystallites resulted by calcination of nitrate precursors. It is interesting to mention that this supplementary porosity has greater contribution in the case of Co_3O_4 than in the case of NiO. This aspect is very important for certain applications, e.g. catalytic and adsorption processes, where the mas transfer plays an important role.

Table 3. Porosity of confined NPs inside the mesopores of SBA-15

Sample	$S_{\mu\,theoretical}$[a] $(m^2.g^{-1})$	$S_{\mu\,exp}$ $(m^2.g^{-1})$	$S_{\mu\,NPs}$ $(m^2.g^{-1})$	$V_{\mu\,theoretical}$[e] $(m^2.g^{-1})$	$V_{\mu\,exp}$ $(m^2.g^{-1})$	$V_{\mu\,NPs}$ $(m^2.g^{-1})$
SBA-15	195	195	0	0.09	0.09	0
CoNi01	86	103	17	0.035	0.042	0.007
CoNi28	75	91	16	0.029	0.036	0.007
CoNi55	73	106	33	0.027	0.039	0.012
CoNi82	82	140	58	0.032	0.054	0.022
CoNi10	84	186	102	0.036	0.08	0.044

[a] $S(V)_{\mu\,theoretical} = S(V)_{BET}-S_{meso}$; [a] $S(V)_{\mu\,exp} > S(V)_{BET}-S(V)_{meso}$;

The morphology of oxide NPs, as well their localization, was analyzed by TEM (Figure 3A-E). In the case of bicomponent samples, TEM was coupled by EDX in order to evaluate quantitatively and qualitatively the chemical composition of those nanoparticles. TEM images show the localization of polycrystalline oxide particles as nanorods inside of pores. Though nor external localization was observed for all the samples, however it could be observed a decrease of particles distribution inside of pores as the cobalt content increases. Thus two extreme situations can be identified. The first one belongs to the sample containing only nickel, when the oxide nanoparticles are rather uniformly distributed within support porosity, whereas the second extreme belongs to the sample containing only cobalt, when relatively large patches could be identified (Figure 3A), confirming thus the results from previous stages of this project. In the first case, the stabilization of NiO nanoparticles is due to both the confinement effect, and chemical interaction between nickel precursor and silica support when nickel phyllosilicates like-phases are formed [4-8]. For cobalt, the phyllosilicates could be also formed, but in smaller amount, fact favoring the migration inside the pores of SBA-15 support with larger aggregates formation. Moreover, our recent published data show that the preparation of cobalt-based NPs by MDI (IWI-MD) method using water as solvent leads to small quantities of phyllosilicates, by comparison with the impregnation in organic solvents (ethanol) or the two solvents methods (this method involves preliminary moistening of support by an hydrophobic organic solvent followed by impregnation with nitrate precursor solved in a water volume smaller than that of pores) [9]. EDX analysis of different oxides nanoparticles indicated both the presence of the two elements in the same particle, while keeping the same mass ratio between as the theoretical one.
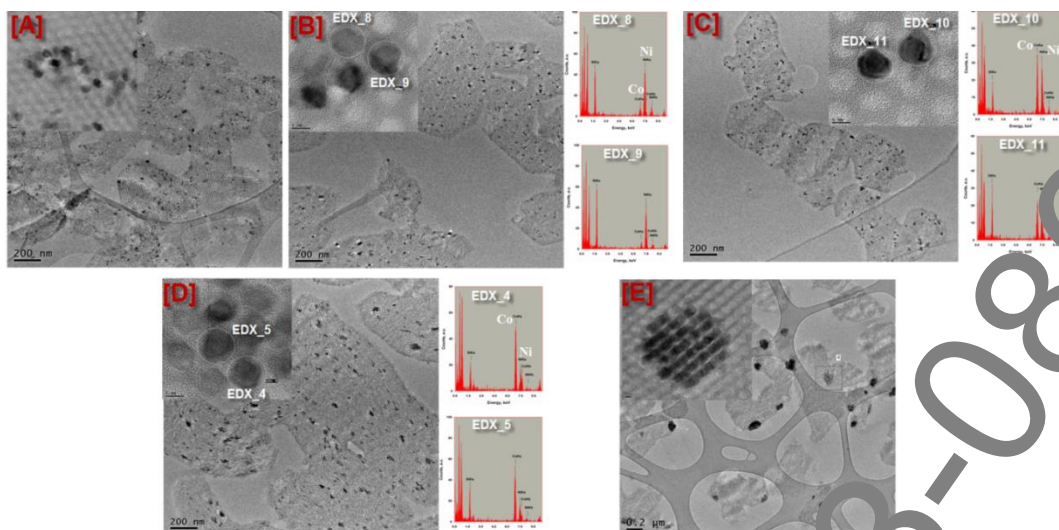
Fig. 3. TEM images for mono-component samples Ni/SBA-15 (A) and Co/SBA-15 (E) and for bi-component CoNi28 (B), CoNi 55(C) and CoNi82 (D) samples together the EDX spectra.

Electronic structure, state of oxidation and degree of coordination of the metallic cations at the surface of nanoparticles prepared in this stage of the project were evaluated by diffuse reflectance UV spectroscopy (DRUV-Vis). In this aim, both the adsorption bands and the band gap energy were analyzed [10]. The band gap energy was correlated with adsorption coefficient from Tauc's relation, $(\alpha h\nu)^n = A(h\nu-E_g)$, where a = adsorption coefficient, A = constant, $h\nu$ = energy of photons, E_g = gap band energy and n = index ranging from ½, 3/2, 2 or 3 depending on the electronic transition responsible for adsorption. For allowed direct transitions n = ½. Since reflectance spectrum is usually registered, the coefficient a is substituted in Tauc's representation by coefficient F(R), resulted from Kubelka Munk transformation. Graphical representation $(F(R)h\nu)^2$ vs. $(h\nu)$ gives a curve having an inflexion point which corresponds to the band gap energy (evaluated by the interception of tangent to this point with x axis). Figure 4 collects UV-vis spectra (A) and Tauc curves (B), while the values of band gaps are shown in Table 4.
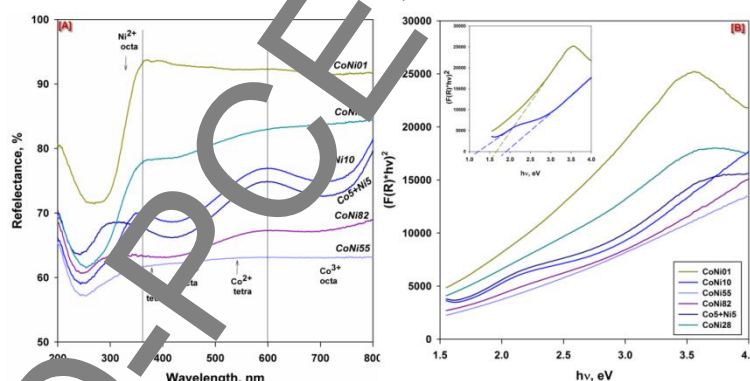

Fig. 4 DR UV-Vis spectra (A) and Tauc curves, $(F(R)*h\nu)^2$ vs. $(h\nu)$ (B) for samples of CoNi/SBA-15 type.

As first remark, all the spectra show an adsorption band at ~250 nm, which is attributed to the charge transfer of type LMCT, $O^{2-} \rightarrow M^{n+}$. Taking into account the adsorption bands from Figure 4A, the sample containing only nickel, CoNi01, shows only a band at ~ 320 nm which is attributed to Ni^{2+} in octahedral coordination, while the sample containing only cobalt show more adsorption bans, with maxima at 235, 410 and 720 nm. The adsorption bands from VIS range are broad, thus indicating the superposition of different bands attributed to Co^{2+} and Co^{3+} species with octahedral and tetrahedral coordination in Co_3O_4 spinel. For bicomponent samples, the registered spectra show the adsorption bands corresponding to both cations. Though, obviously, two or three values of band gap are calculated from UV-vis spectra, the "true" energy of band gap is the corresponding to the value E_{g2}, i.e. at higher wavelengths, usually between 600-800 nm, resulted from electronic transitions d-d from Co 3d-t_{2g} to Co 3d-e_g (or Ni 3d-t_{2g} to Ni 3d-e_g) [13, 17, 20]. Previous studies showed that the particle size and morphology have a major influence on the energy value of the electronic transitions due to the change of network defects [12, 21, 22].

Table 4. Band gap energy calculated on the basis of Tauc curves.

Sample	Eg (eV) [by this project]			Eg (eV) [reported values]	Reference
	Low energy	High energy			
	Eg_1	Eg_2	Eg_3		
CoNi01	-	1.57	3.55	3.6-4.3	11
CoNi28	1.10	-	3.80		
CoNi55	-	1.50	4.40	2.10; 4.30 1.97; 3.40 2.6; 2.63	12 13
CoNi82	1.05	1.82	4.30		
CoNi10	1.18	1.91	4.35	2.38; 2.52; 3.44 1.50-2.50 2.22; 3.55 1.48; 2.19 1.50; 2.00 1.77; 3.15 1.70; 2.85 1.75-1.92; 3.15-3.4 1.43-1.51; 1.5-1.9	2 14 15 16 17 18 19 20

Thus, as the particle size is smaller, the electron excitation occurs at higher energy. Analysing data from Table 4, it could be observed that the energy of band gap (Eg_2) increases with increasing oxide crystallite, contrary to literature data. Anyway, the range of crystallites size is rather small (7.9-13.7 nm) to observe an influence of the crystallite size on the value of band gap. An increase in this energy with increasing of cobalt amount is also observed. If the TEM images are considered, showing the agglomeration of particles as the amount of cobalt increases, it could be affirmed that the aggregation of nanoparticles as patches would require higher energy as the electronic excitation to take place. However, our results are in line with the most part of the published data, and they recommend the cobalt based materials, prepared as described in this project, to be use also in other applications than the catalytic ones, like: optical and gas sensors, electrochromic materials, adsorption of solar energy, optoelectronic materials, photocatalysts etc.

The original results of studies carried out in this project were the subject of 3 ISI publications[9,23,24] and 6 communications at international symposiums.

References
1. Zhang, F; Yan, Y; Yang, H; Meng, Y; Yu, C; Tu, B; Zhao, D. *J. Phys. Chem. B,* 2005, **109**, 8723.
2. Zhu, Y; Ji, X; Wu, Z; Song, W; Hou, H; Wu, Z; He, X; Chen, Q; Banks, C.E. *J. Power Sources,* 2014, **267**, 888
3. Sietsma, JRA; Meeldijk, JD; Versluijs-Helder, M; Broersma, A; van Dillen, AJ; de Jongh, PE; de Jong, KP. *Chem. Mater.*, 2008, **20**, 2921
4. Dumitriu, E; Raport stiintific privind implementarea proiectului PN-II-ID-PCE-2011-3-0868, (2013).
5. Galarneau A; Cambon, H; Di Renzo, F; Ryoo, R; Choi, M; Fajula, F; *New J. Chem.*, 2003, **27**, 73.
6. Dumitriu, E; Raport stiintific privind implementarea proiectului PN-II-ID-PCE-2011-3-0868, (2012).
7. Ungureanu, A; Dragoi, B; Chirieac A; Royer, S; Duprez, D; Dumitriu, E. *J. Mater. Chem.*, 2011, **21**, 12529.
8. Ungureanu, A.; Dragoi, B.; Chirieac, A.; Ciotonea, C.; Royer, S.; Duprez, D.; Mamede, A.S.; Dumitriu. E. *ACS Appl. Mater. Interfaces*, 2013, **5**, 3010
9. Dragoi, B; Ungureanu, A; Ciotonea, C, Chirieac, A; Petit, S; Royer, S; Dumitriu, E. *Microporous and Mesoporous Mater.,* 2015, DOI: 10.1016/j.micromeso.2015.11.028.
10. Herrera, JE; Resasco, DE. *J. Phys. Chem. B*, 2003, **107**, 3738.
11. Mohseni Meybodi, S; Hosseini, S.A; Rezaee, M; Sadrnezhaad, S.K; Mohammadyani, D, *Ultrasonics Sonochemistry,* 2012, **19**, 841.
12. Anu Prathap, M.U; Wei C; Sun, S; Xu, ZJ. *Nano Research,* 2015 DOI: 10.1007/s12274-015-0769-z.
13. Anu Prathap, M.U; Srivastava, R. *Nano Energy* 2013, **2**, 1046.
14. Qiao L; Xiao H.Y; Meyer, H.M; Sun, J.N; Rouleau, C.M; Puretzky, A.A; Geohegan, D.B; Ivanov, I.N; Yoon, M; Weber, W.J; Biegalski, M.D, *J. Mater. Chem. C*, 2013, **1**, 4628.
15. Farhadi, S; Safabakhsh, J; Zaringhadam P, *J. Nanostruc. Chem.*, 2013, **3**, 69.
16. Patil, V; Joshi, P; Chougule M; Sen, S, *Soft Nanosci. Lett.*, 2012, **2**, 1.
17. Barreca, D; Massignan, C; Daolio, S; Fabrizio, M; Piccirillo, C; Armelao, L; Tondello, E, *Chem. Mater.*, 2001, **13**, 588.
18. Gu, F; Li, C; Hu, Y; Zhang, L, *J. Crystal Growth*, 2007, **304**, 369.
19. Sarfraz, A.K; Hasanain, S.K, *Acta Phys. Polonica A*, 2014, **125**, 139.
20. Roy, M; Ghosh, S; Kanti Naskar, M, *Phys.Chem.Chem.Phys.*, 2015, **17**, 10160
21. Sattler, K, Nalwa H.S. (Ed.) in *Handbook of Thin Films Materials, vol. 5: Nanomaterials and Magnetic Thin Films,* 2002, Academic Press.
22. Xiao H.-Y; Fu S.-Y; Zhu, L.-P; Li Y.-Q; Yang, G, *Eur. J. Inorg. Chem.*, 2007, 1966.
23. Audemar, M; Ciotonea, C.; De Oliveira Vigier K.; Royer, S.; Ungureanu, A.; Dragoi, B.; Dumitriu, E.; Jérôme, F., *ChemSusChem*, 2015, **8**, 1885.
24. Rudolf, C; Abi-Ghaida, F; Dragoi, B; Ungureanu, A; Mehdi, A; Dumitriu, E, *Catal. Sci. Technol.*, 2015, **5**, 3735

Project leader,

Prof.dr.ing. Emil DUMITRIU